Mechanical anisotropy and multiple direction-dependent Dirac states in a synthesized Ag_3C_{20} monolayer

Zhiheng Lv [1], Ningning Jia,[1] Jiangtao Cai,[2] Xue Jiang,[3] Jijun Zhao,[3,*] and Zhifeng Liu [1,†]

[1]*Inner Mongolia Key Laboratory of Nanoscience and Nanotechnology, School of Physical Science and Technology, Inner Mongolia University, Hohhot 010021, China*

[2]*Department of Physics, Shaanxi University of Science and Technology, Xi'an 710021, China*

[3]*Key Laboratory of Materials Modification by Laser, Ion and Electron Beams (Dalian University of Technology), Ministry of Education, Dalian 116024, China*

Recently, a two-dimensional (2D) orthorhombic silver-organic framework, Ag_3C_{20} monolayer, was synthesized by assembling organic molecules linked with multiple aryl-metal bonds. Using first-principles calculation, herein we demonstrate that, owing to the unique bonding feature, Ag_3C_{20} monolayer not only exhibits strong mechanical anisotropy, but also possesses rich orientation-dependent Dirac states allowing for modulation via external means. Around the Fermi level below, the intrinsic Dirac points form two quasi-type-III nodal lines protected by mirror symmetry, which can further evolve into hybrid nodal loops under tiny strains. Intriguingly, a peculiar semi-Dirac state near the Fermi level above emerges under a critical strain by merging two type-I Dirac cones, which harbors direction-dependent strongly localized fermions, normal massive carries, and ultrafast Dirac fermions at the same time. These findings suggest that the mechanically sensitive Ag_3C_{20} monolayer is a promising 2D material to realize the interesting Dirac physics and multiple carrier transport with high anisotropy.

I. INTRODUCTION

Two-dimensional (2D) Dirac materials hosting linear band dispersion near the Fermi level like that of graphene [1] have attracted great attention due to many exotic physical phenomena and properties [2–4] (e.g., ballistic transport, high carrier mobility, and topological phases) associated with the Dirac states. For versatile applications, the tailorable band dispersions are highly desirable [5], which in turn modulate the group velocities of charge carriers. Beyond the isotropic 2D Dirac materials, more and more efforts [5–11] have been devoted to the 2D systems with anisotropic Dirac band dispersions, such as the graphene superlattices [5,6], 6,6,12-graphyne [7], OPG-Z [8], phagraphene [9], S-graphyne [10], and χ_3 borophene [11].

In terms of the anisotropic band dispersions, Dirac nodal line [12–14] and semi-Dirac [15–18] semimetals are particularly outstanding among 2D Dirac materials. For the former, their Dirac points form extended lines in the 2D Brillouin zone (BZ) [14–20]. Due to the continuity of the Dirac points, band dispersions near them are highly anisotropic, at least quite different along the tangential and transverse directions, like the case of three-dimensional (3D) nodal line semimetals [21]. As is known, the linear dispersion along a certain k path can be usually classified into three scenarios: (i) the slopes of the two crossing bands are opposite in sign, termed as type-I Dirac dispersion; (ii) the slopes share the same sign, i.e., type II;

(iii) the slope of one linear band is equal to zero, while that of the other one is nonzero, i.e., type III. According to these Dirac dispersions, there are three types of nodal lines, namely type-I, -II, and -III nodal lines [22], in which the band dispersion along transverse direction of the nodal line are type-I, -II, and -III Dirac dispersions, respectively.

The semi-Dirac state exhibits a massless linear dispersion along one principal axis, but massive quadratic dispersion in another perpendicular axis [15,16]. Such particular band dispersions make the semi-Dirac materials not only have highly anisotropic transport properties [23] but also exhibit many interesting physical phenomena, e.g., non-Fermi liquid behavior [24], unusual Landau levels [25,26], and quantum thermoelectric effect [27]. In past few years, some real materials have been confirmed to harbor Dirac nodal line [19,28–32] or semi-Dirac states [16,17,33]. What is more, the coexistence of them have also been theoretically proven to be possible [18], which is much desired for the device applications with greater flexibility. However, in the only known hypothetical system, hexagon- and rhombus-stripe boron (hr-B) [34], one cannot obtain the clean Dirac nodal line fermions and semi-Dirac fermions because of the mutual contamination between them in the same energy window. Naturally, two unsolved issues arise: First, can these anisotropic Dirac states can coexist with energy separation around the Fermi level in a real material that can be synthesized? Second, can the states can be tailored by applying external means that are feasible in experiment?

Beyond the traditional organometallic frameworks, Chi *et al.* [35] recently synthesized an interesting 2D metal-organic hybrid, Ag_3C_{20} monolayer (ML), which is assembled by organic molecules linked via multiple aryl-metal bonds

---

*zhaojj@dlut.edu.cn
†zfliu@imu.edu.cn

(*bay*-aryl-metal and *peri*-aryl-metal bonds) rather than single aryl-metal bonds. The incorporation of multiple aryl-metal bonds not only increases the diversity of 2D metal-organic hybrids but also raises a question worthy of exploring: can the coexistence of multiple aryl-metal bonds induces interesting anisotropic physics, especially in aspect of the aforementioned Dirac electronic states?

To address all these issues, we systematically investigate the mechanical and electronic properties of Ag_3C_{20} ML using first-principles calculations. Our results reveal that Ag_3C_{20} ML is strongly anisotropic in both mechanical and electronic behavior. Remarkably, Dirac nodal line and semi-Dirac states are simultaneously obtained in Ag_3C_{20} ML in an easily tunable way, and they reside on the different sides of the vicinity of the Fermi level without energy overlap. Therefore, it would be possible to switch between these two types of Dirac states through opposite gate voltages, thereby achieving the desirable clean anisotropic carrier transport in Ag_3C_{20} ML based nanodevices.

II. COMPUTATIONAL METHODS

All first-principles calculations are performed with the Vienna *Ab initio* Simulation Package [36]. The projector augmented wave (PAW) method [37] is adopted to deal with the core-valence interactions, taking a cutoff energy of 500 eV for the plane-wave basis. The Perdew-Burke-Ernzerhof (PBE) [38] functional within the generalized gradient approximation (GGA) is employed to describe the exchange-correlation interactions. A Monkhorst-Pack k-point mesh with uniform spacing of $2\pi \times 0.02$ Å^{-1} is used to sample the 2D BZ. To avoid the interactions between the adjacent periodic images, a 20 Å vacuum layer is applied along the perpendicular direction of the 2D ML structure. The convergence criterion of electronic iteration is set to 10^{-6} eV, and the structure is relaxed until Hellmann-Feynman force on each atom is less than 0.01 eV/Å. For band-structure calculations, a more accurate hybrid functional HSE06 [39] is also employed on the basis of PBE-optimized geometry.

III. RESULTS AND DISCUSSION

A. Atomic structure and bonds

Without any lattice constraint, the freestanding Ag_3C_{20} ML is fully relaxed to be a completely planar structure in an orthorhombic lattice with *Pmmm* symmetry (No. 47), as shown in Fig. 1(a). The equilibrium lattice parameters are $a = 1.14$ nm and $b = 0.83$ nm, which are quite consistent with the experiment results [35] of $a = 1.16 \pm 0.02$ nm and $b = 0.86 \pm 0.02$ nm, respectively. This means that the chosen computational strategy is suitable for Ag_3C_{20} ML. In the primitive cell [see the shadow area in Fig. 1(a)], there is a complete perylene [40] skeleton formed by five C_6 rings with 20 C atoms, sharing four Ag atoms at the *peri*-positions along the *a* axis and two Ag atoms at the *bay*-positions along the *b* axis. As a consequence, there exist two kinds of aryl-metal bonds [35], i.e., *peri*-Ag-C bonds (2.11 Å) and *bay*-Ag-C bonds (2.15 Å), interlinking the isolated perylene motifs to construct the periodic framework of Ag_3C_{20} ML. The calculated electron localization function [41] (ELF) in Figs. 1(b)
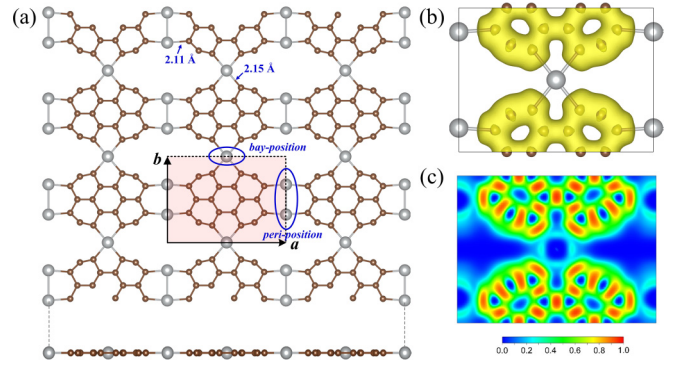

FIG. 1. (a) Top and side views for the optimized atomic structure of Ag_3C_{20} ML. The magenta shadow area denotes the primitive cell. (b) The top view of the electron localization function (ELF) for Ag_3C_{20} ML with isosurface of 0.72. (c) The 2D slice of ELF for a horizontal plane through the atomic center in panel (b). Here, the site with ELF = 0 has no electron distribution, while that with ELF = 1.0 holds a completely localized electron.

and 1(c) suggest that both *peri*- and *bay*-Ag-C bonds belong to ionic interaction with C atoms as the electron acceptor. As a whole, the bonding strength along the *a* axis depends on the ionic *peri*-Ag-C and armchair covalence C–C bonds in perylene motifs, and that along the *b* axis upon the *bay*-Ag-C and zigzag C–C bonds. In view of such interesting structural features, hereafter we will focus on the anisotropy of Ag_3C_{20} ML in both mechanical and electronic properties, and the possible interplay between them.

B. Mechanical anisotropy

To explore the mechanical properties of Ag_3C_{20} ML, we first examine its elastic strain energy $U(\varepsilon)$ per unit area caused by in-plane strains, which can be expressed as [42]

$$U(\varepsilon) = \tfrac{1}{2}C_{11}\varepsilon_{xx}^2 + \tfrac{1}{2}C_{22}\varepsilon_{yy}^2 + \tfrac{1}{2}C_{12}\varepsilon_{xx}\varepsilon_{yy} + 2C_{66}\varepsilon_{xy}^2. \quad (1)$$

For the current 2D system, the standard Voigt notation [43] (1-*xx*, 2-*yy*, and 6-*xy*) is used. In this manner, elastic constants C_{ij} can be derived by fitting the strain energy curves under different strains ε_{ij}. As seen from Figs. 2(a) and 2(b), the energy response to applied strain is anisotropic in Ag_3C_{20} ML, which is reflected by the large difference among the fitted elastic constants (e.g., $C_{11} = 108.83$ N/m vs $C_{12} = 2.26$ N/m, and $C_{22} = 48.65$ N/m vs $C_{66} = 7.57$ N/m). To examine the directional dependence of mechanical strength in details, we then evaluate Young's modulus $Y(\theta)$ and Poisson's ratio $v(\theta)$ from the obtained elastic constants [44]:

$$Y(\theta) = \frac{C_{11}C_{22} - C_{12}^2}{C_{11}s^4 + \left(\frac{C_{11}C_{22} - C_{12}^2}{C_{66}} - 2C_{12}\right)s^2c^2 + C_{22}c^4}, \quad (2)$$

$$v(\theta) = -\frac{\left(C_{11} + C_{22} - \frac{C_{11}C_{22} - C_{12}^2}{C_{66}}\right)s^2c^2 - C_{12}(s^2 + c^4)}{C_{11}s^4 + \left(\frac{C_{11}C_{22} - C_{12}^2}{C_{66}} - 2C_{12}\right)s^2c^2 + C_{22}c^4}, \quad (3)$$

where θ is the polar angle with respect to the *a* axis; s and c are abbreviations for $\sin(\theta)$ and $\cos(\theta)$, respectively. The calculated $Y(\theta)$ and $v(\theta)$ of Ag_3C_{20} ML are displayed in Figs. 2(c) and 2(d), respectively. With the increasing of θ, ranging from $0°$ (*a* axis) to $90°$ (*b* axis), the Young's modulus first decreases
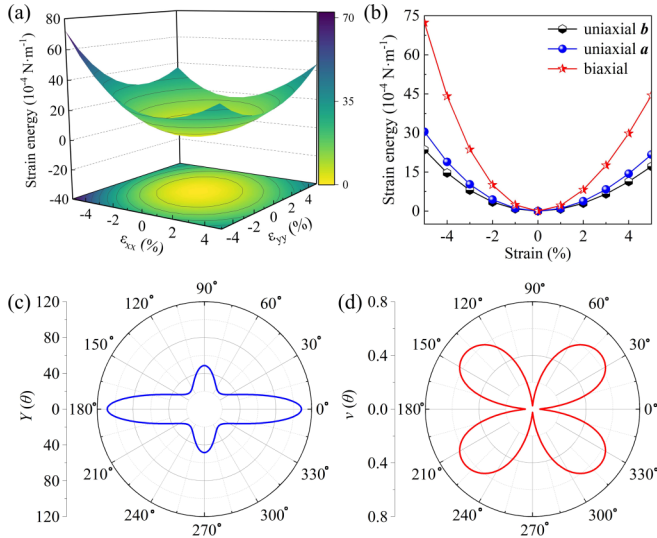
FIG. 2. (a) The strain energies $U(\varepsilon)$ per unit area for Ag_3C_{20} ML with respect to a ε_{xx}-ε_{yy} strain plane in the range of -5%–5%, together with the corresponding 2D contour plot. (b) The strain energies $U(\varepsilon)$ as a function of the uniaxial a/b and biaxial strains. As is shown, the easiest energy change occurs under the biaxial strains, followed by the uniaxial b strains, and then the uniaxial a strains. (c) $Y(\theta)$ and (d) $\nu(\theta)$ of Ag_3C_{20} ML in polar diagrams.
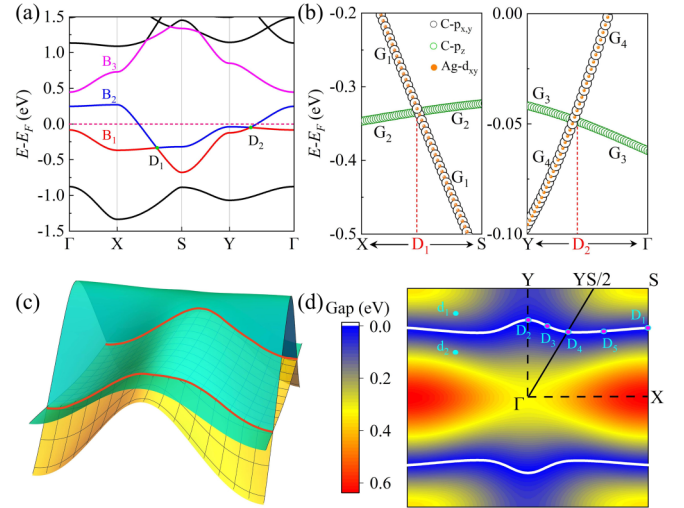

FIG. 3. (a) The electronic band structure of pristine Ag_3C_{20} ML. (b) The orbital and atom decomposed bands with irreducible representations around the Dirac points of D_1 and D_2. (c) The 3D band structure in the entire first BZ. (d) The contour plot of the energy band gap between bands B_1 and B_2.

from the maximal value (108.69 N/m at $\theta = 0°$) to the minimal value (24.86 N/m at $\theta = 45°$) and then increases to a relatively smaller value (48.58 N/m at $\theta = 90°$). The ratio between the maximum and minimum of Young's modulus is about 4.41, evidently larger than that of the two typical anisotropic 2D carbon-based materials W-graphane (≈ 2.62) [44] and palgraphyne (≈ 3.29) [45]. In this sense, Ag_3C_{20} ML can be regarded as a strong mechanically anisotropic 2D material. Moreover, from the Poisson ratios in Fig. 2(d), one can derive a consistent conclusion. In contrast with Young's modulus, the Poisson ratios, appearing as a flower petal, have the maximal value of 0.652 in $\theta = 45°$ direction, while it holds vanishingly small values along the principle a and b axes. It should be noted that the ratio ($0.0539/0.0241 = 2.24$) between the Poisson ratios of the a and b axes is still consistent with that ($108.69/48.58 = 2.24$) of Young's modulus.

C. Topological nodal lines and direction-dependent Dirac dispersions

The electronic band structure depicted in Fig. 3(a) reveals that Ag_3C_{20} ML is a metal having a partially filled conduction band. Right below the Fermi level, the denoted bands B_1 and B_2 meet at two points, namely D_1 (0.5, 0.30723) along the path X → S and D_2 (0, 0.3403) along Γ → Y, with the low-energy bands exhibiting linear dispersion. Since one of the linear bands is almost flat, the band dispersion around both D_1 and D_2 can be referred to as quasi-type-III Dirac dispersion, which appears in a certain direction of type-III Dirac cones [46,47] and the transverse direction of type-III nodal lines [48]. To understand the origin of the Dirac states, we calculate the orbital and atom decomposed bands near D_1 and D_2. As illustrated in Fig. 3(b), the wave functions near the

Dirac points are mainly contributed by the $p_{x,y}$ and p_z orbitals of C atoms, together with little portion from Ag-d_{xy} orbitals. Obviously, the energy ordering switches between C-$p_{x,y}$ and C-p_z bands. In fact, such kind of band inversion is one of the key features for topological semimetals or metals [49,50]. Note that, (i) as the band crossings are mainly formed by the lightweight C atoms, the spin-orbit coupling (SOC) effect is quite weak [≈ 10 meV, see Fig. S1(a) in the Supplemental Material [51]], which will be ignored in our following discussion; (ii) the confirmed Dirac band dispersion without SOC can be also reproduced in more accurate HSE06 calculations [Fig. S1(b) in the Supplemental Material [51]].

The identified multicrossing Dirac points are reminiscent of the Dirac nodal lines [12,13], which is composed of consecutive Dirac points. To reveal the complete pattern of the Dirac points, we plot 3D band structure of Ag_3C_{20} ML in the entire BZ, as presented in Fig. 3(c). The results confirm that B_1 and B_2 bands meet with each other along two open M-shaped nodal lines with mirror symmetry, running across the whole BZ [Fig. 3(d)] along the k_x-axis direction. Since all the band dispersions along the transverse direction of the nodal lines belong to quasi-type III, one can conclude that Ag_3C_{20} ML is a quasi-type-III nodal line metal. To elucidate how these nodal lines form, we further carry out symmetry analysis for the crossing B_1 and B_2 bands of Ag_3C_{20} ML using the IRVSP code [52]. Around D_1 and D_2 in the highly symmetric paths, the irreducible representations of the two crossing bands are G_1 and G_2, and G_3 and G_4, respectively [see Fig. 3(b)]. As for other general Dirac points [e.g., the arbitrary D_3, D_4 and D_5 in Fig. 3(d)], which are not located on the high-symmetry line, the identified representations are all G_1 and G_2, as shown in Fig. S2 in the Supplemental Material [51]. With the help of Bilbao Crystallographic Server [53], we confirm that common symmetrical operator corresponding to these representations is m_{001} mirror symmetry, belonging to the second-order point group C_s. Therefore, the nodal lines in Ag_3C_{20} ML are caused
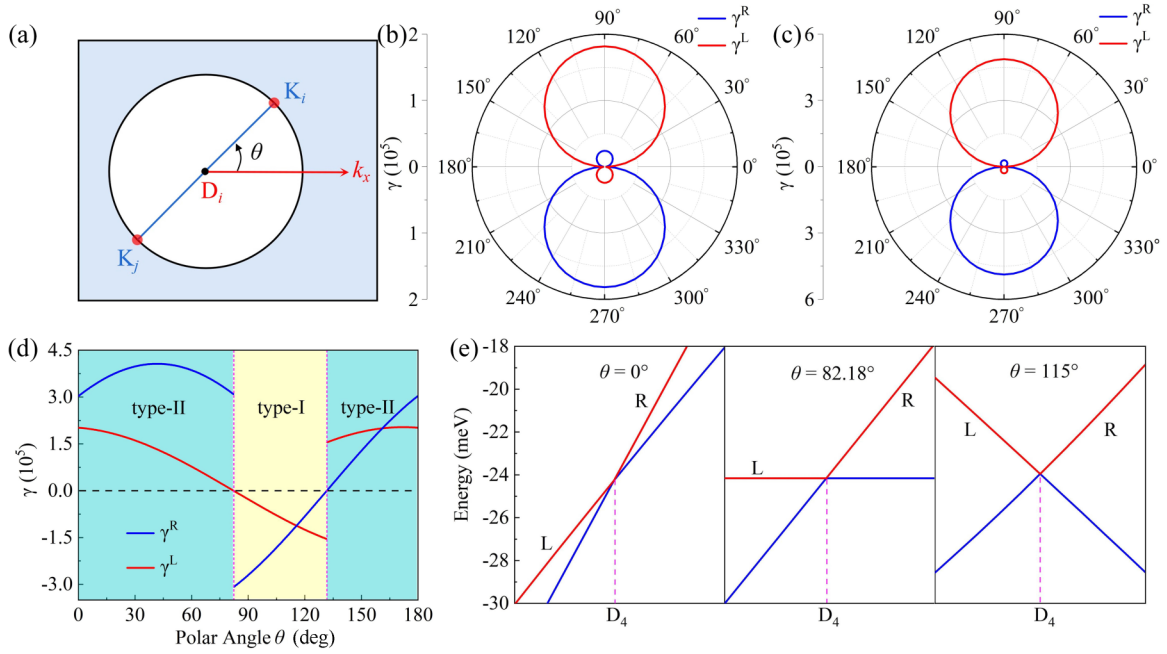
FIG. 4. (a) The schematic diagram of the polar coordinate in the 2D momentum space with the Dirac point D_i ($i = 1, 2, 4$) as the origin. The distribution of the slope indexes γ^L and γ^R along different $\boldsymbol{k}$ directions (θ) for (b) D_1, (c) D_2, and (d) D_4. (e) The low-energy band structures around the Dirac point D_4 along the $\boldsymbol{k}$ paths of $\theta = 0°$, 82.18°, and 115°.

by the band inversions between C $p_{x,y}$ and C p_z, protected by mirror reflection symmetry.

Owing to the mechanism of mirror-symmetry protection, the topological properties of Ag_3C_{20} ML should be characterized by the topological invariant ζ_0, which is suitable for type-A topological nodal line semimetals [54]. In the BZ plane, we first pick up two $\boldsymbol{k}$ points [i.e., d_1 and d_2, see Fig. 3(d)] on different sides of the nodal line. Subsequently, we count the number of bands below the energy of Dirac point with the mirror eigenvalue of $+1$ at d_1 and d_2 (see Table S1 in the Supplemental Material [51]), which are denoted by N_1 (41) and N_2 (40), respectively. Finally, the topological invariant is evaluated to be 1 using $\zeta_0 = N_1 - N_2$. Hence, the linear crossings of the nodal lines in Ag_3C_{20} ML should not be accidental as long as the mirror symmetry is preserved, they will not be opened up by an arbitrarily small perturbation.

To demonstrate the anisotropy of the lower-energy band dispersions around nodal points in the nodal line [taking D_1, D_2, and D_4 as examples, see Fig. 3(d)], we further calculate the band structures along the possible $\boldsymbol{k}$ paths except for the tangent directions of the nodal line. As schematically shown in Fig. 4(a), 1000 $\boldsymbol{k}$ paths, characterized by $K_i \rightarrow K_j$ and polar angle θ, are sampled uniformly in a polar coordinate system with respect to the k_x axis. On the basis of the obtained 1000 band structures, the slope indexes defined as $\gamma^R = v_F^R \,\text{sgn}(v_F^L)$ and $\gamma^L = v_F^L \,\text{sgn}(v_F^R)$ [55] are employed to describe the band dispersion features. Here "L" and "R" indicate the left and right Dirac bands, respectively [like that in Fig. 4(e)]; v_F represents Fermi velocity for the corresponding linear bands, which can be evaluated from the equation of $\hbar v_F = dE(\boldsymbol{k})/d\boldsymbol{k}$. Figures 4(b) and 4(c) show the slope indexes γ^f ($f = L$ or R) as a function of the polar angle θ for the low-energy bands around D_1 and D_2, respectively. Two common characteristics are observed: (i) both γ^R and

γ^L are positive in all of the considered $\boldsymbol{k}$ paths, which means that the slopes of the two bands share the same sign, and the Dirac dispersion should belong to type I (or quasi-type III, see following characteristic) along the corresponding $\boldsymbol{k}$ path; (ii) the dispersion of the two bands is quite different one is almost dispersionless with effective mass far less than that of the other. As for the case of D_4, the most important feature is that there exists a change in the sign of γ^f, as illustrated in Fig. 4(d). Namely, the type of Dirac dispersions have been completely changed with the variation of the $\boldsymbol{k}$ paths. Specifically, as θ increases from 0° to 180°, the band dispersion changes from type II to type I, and then to type II again. In the transition boundary between them, the type-III dispersion with one dispersionless band is found at two critical directions ($\approx 82.18°$ and $\approx 131.9°$). A more direct visualization can be seen in the low-energy band structures along three representative directions [see Fig. 4(e)], i.e., $\theta = 0°$, 82.18°, and 115°, showing the features of type-II, type-III and type-I Dirac dispersions, respectively.

D. Strain-induced nodal line evolution and semi-Dirac state

As is known, applying external strain is an effective approach for engineering the electronic properties of 2D materials [56,57]. In consideration of the strong anisotropy of mechanical properties, we apply uniaxial (**a** axis or **b** axis) and biaxial strains ranging from −5% to 5% (which are accessible in experiments [56]) for Ag_3C_{20} ML and relax all the atomic positions by fixing the strained lattice parameters. After optimization, we recalculate the electronic band structure for each strained structure of Ag_3C_{20} ML, as illustrated in Figs. S3–S5 in the Supplemental Material [51]. The results reveal that the electronic bands of Ag_3C_{20} ML is mechanically sensitive. Under different strains, some intriguing electronic
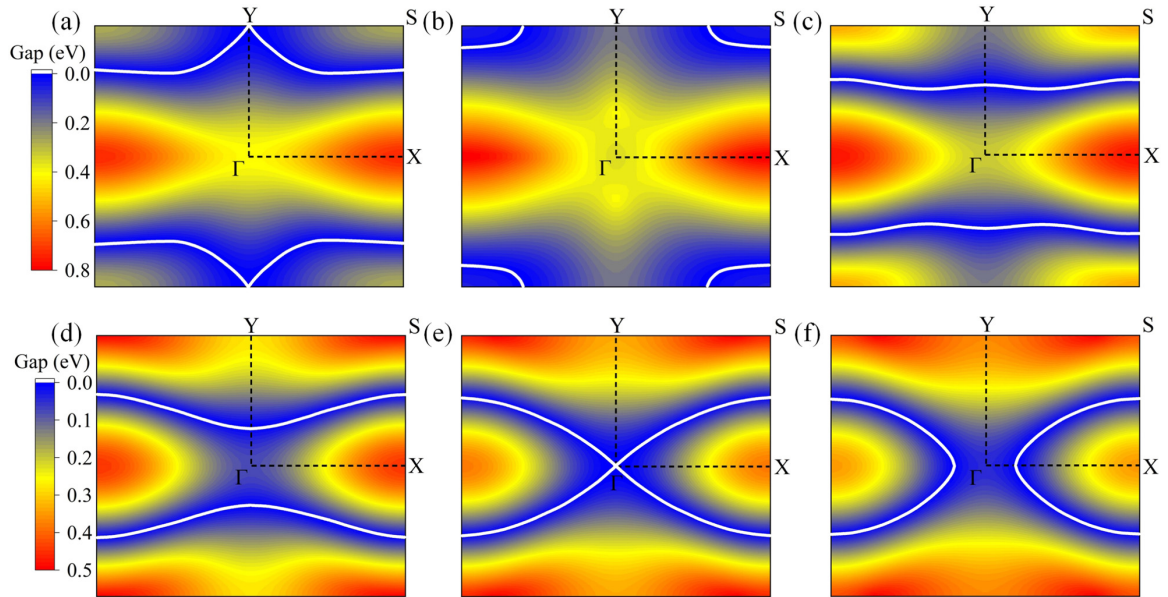
FIG. 5. The contour plot of energy gap between bands B_1 and B_2 under different strains: (a) -0.8% biaxial strain, (b) -3% biaxial strain, (c) 1% uniaxial **b** strain, (d) 3% uniaxial **b** strain, (e) 4.2% uniaxial **b** strain, (f) 5% uniaxial **b** strain.

states emerge around the Fermi level. In the following, we focus on two aspects: (i) evolution of nodal lines formed by B_1 and B_2 below the Fermi level, and (ii) the Dirac cone and semi-Dirac state formed by B_2 and B_3 above the Fermi level.

Evolution of the nodal lines. Under the three types of compressive strains, the two nodal lines shift along opposite direction along k_y axis. After they touch the BZ boundary at the high-symmetry Y or Y' point under a critical strain (about 0.8%, 1.5%, and 2.2% for biaxial, uniaxial **b**, and uniaxial **a** strains, respectively), their geometries transform from the two open lines into one closed loop [see Figs. 5(a) and 5(b)]. More specifically, it is a hybrid nodal loop centered at the corner point S, exhibiting both type-III and type-II Dirac dispersions along its transverse directions, as displayed in the bands along $X \to S$ and $Y \to S$, respectively (Figs. S3–S5 in the Supplemental Material [51]). With the increase of compressive strains, the nodal loop will gradually shrink. By biaxial strains, the loop will eventually disappear when the strain is larger than 3.5%, which, however, will not happen in the uniaxial cases due to anisotropy.

In the case of uniaxial **a** tensile strain, the quasi-type-III nodal lines remain almost unchanged. However, interesting evolution behavior are found in the other two types of strains. With the increase of uniaxial **b** and biaxial strains, the two nodal points in the k_y axis gradually move towards Γ and meet with each other at the BZ center under $\approx 4.2\%$ [Fig. 5(e)] and $\approx 5\%$ for uniaxial **b** and biaxial strains, respectively. On the contrary, the nodal points in $X \to S$ and $X' \to S'$ are almost fixed. Because of such difference in mechanical response, the nodal lines can be tuned from two curves protruding towards Y to two approximately parallel quasistraight lines with slight fluctuations [Fig. 5(c)], and then to two curves protruding towards the opposite direction [Fig. 5(d)]. Moreover, under uniaxial **b** strains ($>4.2\%$) [Fig. 5(f)], the two open lines also evolve into one closed loop, but centered at the X/X' points.

Dirac cones and semi-Dirac state. Finally, we discuss B_2 and B_3 bands slightly above the Fermi level. There is a sizable band gap between B_2 and B_3 bands for all the considered uniaxial **a** strains in either tensile or compressive case. Under modest uniaxial **b** and biaxial strains, however, the two gapped bands will cross with each other, and form some intriguing isolated Dirac cones. Such difference in band change stems from the fact that B3 band is mainly contributed C-p_y orbitals (see Fig. S7 in the Supplemental Material [51]). As illustrated in Figs. 6(a) and 6(b), two pair of isolated Dirac
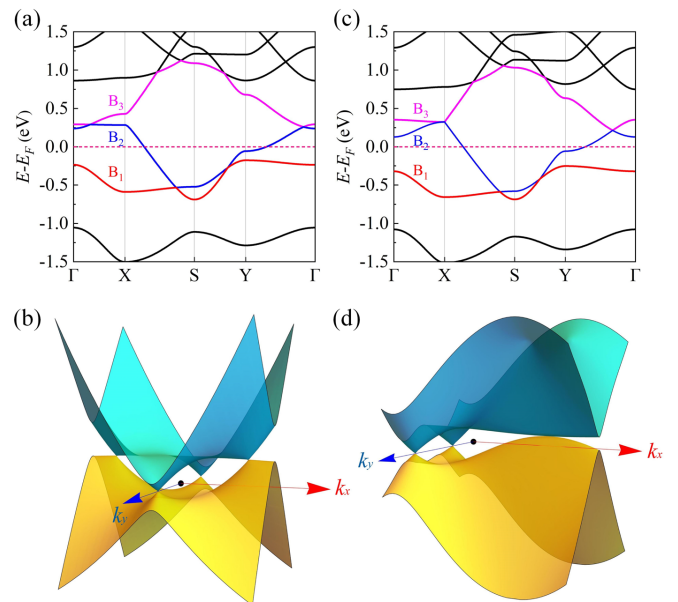

FIG. 6. The electronic band structures of Ag_3C_{20} ML under -2% biaxial strain (a) and -3% biaxial strain (c); the corresponding 3D plots of B_2 and B_3 bands are presented in (b) and (d), respectively.

cones are induced when the compressive biaxial (uniaxial *b*) strain is larger than $\approx 1.2\%$ ($\approx 2.0\%$). As the strain continues to increase, the two coupled Dirac cones along k_x axis merge together and form a semi-Dirac cone [15,16] at the X point [see Figs. 6(c) and 6(d)] under a critical strain of 3% for the biaxial case (4.2% for uniaxial *b*). Unlike the conventional Dirac cone, the semi-Dirac state exhibits strong dispersion anisotropy, having the standard type-I Dirac dispersion along the X $\rightarrow$ S path, but quadratic dispersion in the perpendicular X $\rightarrow$ Γ path. Uniquely, along the X $\rightarrow$ Γ direction one can find that the B3 band is almost dispersionless, shaped like a quasi flat band. In this regard, the identified semi-Dirac cone of the strained Ag_3C_{20} ML should be referred to as *extreme semi-Dirac cone* due to the coexistence of massless linear band and superheavy quasi flat band (see Fig. S6 in the Supplemental Material [51]), which has extreme effective mass, ranging from zero to infinity. In practical device application, three types of fermions with distinctly different carrier transport velocities should be obtained in their respective directions, including superheavy localized fermions, conventional massive carries, and ultrafast massless Dirac fermions. With the strain increasing further, the semi-Dirac cone disappear, but the two isolated Dirac cone along the k_y axis can still be preserved up to 5% compressive strains in both uniaxial *b* and biaxial cases.

IV. CONCLUSION

To summarize, we have performed a systematical first-principles study on the mechanical and electronic properties of the recently synthesized Ag_3C_{20} ML. Our results show that Ag_3C_{20} ML has strong mechanical anisotropy due to its particular structure constructed by multiple aryl-metal bonds. Associated with this, it also hosts two types of desirable Dirac states, including Dirac nodal line and semi-Dirac cone with highly anisotropic band dispersions. Specifically, its intrinsic Dirac points form two M-shaped nodal lines right below the Fermi level. Moreover, around certain Dirac points of the nodal lines, type-I, -II, and -III Dirac dispersions are found in the low-energy bands. Under a modest strain, the open nodal lines can evolve into a closed hybrid nodal loop, and an unprecedented semi-Dirac cone can be induced above the Fermi level, which holds multiple direction-dependent fermions, including superheavy localized fermions, normal massive carries, and ultrafast massless Dirac fermions. Given these, we believe that the synthesized Ag_3C_{20} ML should be a promising platform for constructing flexible nanodevices exhibiting interesting topological physics and highly anisotropic Dirac carries transport.

[1] K. S. Novoselov, A. K. Geim, S. V. Morozov, D. Jiang, M. I. Katsnelson, I. V. Grigorieva, S. V. Dubonos, and A. A. Firsov, Two-dimensional gas of massless Dirac fermions in graphene, Nature (London) **438**, 197 (2005).

[2] J. Wang, S. Deng, Z. Liu, and Z. Liu, The rare two-dimensional materials with Dirac cones, Natl. Sci. Rev. **2**, 22 (2015).

[3] R. Fan, L. Sun, X. Shao, Y. Li, and M. Zhao, Two-dimensional Dirac materials: Tight-binding lattice models and material candidates, ChemPhysMater, doi: 10.1016/j.chphma.2022.04.009.

[4] T. Wehling, A. Black-Schaffer, and A. Balatsky, Dirac materials, Adv. Phys. **63**, 1 (2014).

[5] S. Rusponi, M. Papagno, P. Moras, S. Vlaic, M. Etzkorn, P. M. Sheverdyaeva, D. Pacilé, H. Brune, and C. Carbone, Highly Anisotropic Dirac Cones in Epitaxial Graphene Modulated by an Island Superlattice, Phys. Rev. Lett. **105**, 246803 (2010).

[6] C.-H. Park, L. Yang, Y.-W. Son, M. L. Cohen, and S. G. Louie, Anisotropic behaviours of massless Dirac fermions in graphene under periodic potentials, Nat. Phys. **4**, 213 (2008).

[7] D. Malko, C. Neiss, F. Viñes, and A. Görling, Competition for Graphene: Graphynes with Direction-Dependent Dirac Cones, Phys. Rev. Lett. **108**, 086804 (2012).

[8] C. Su, H. Jiang, and J. Feng, Two-dimensional carbon allotrope with strong electronic anisotropy, Phys. Rev. B **87**, 075453 (2013).

[9] Z. Wang, X. F. Zhou, X. Zhang, Q. Zhu, H. Dong, M. Zhao, and A. R. Oganov, Phagraphene: A low-energy graphene allotrope composed of 5-6-7 carbon rings with distorted Dirac cones, Nano Lett. **15**, 6182 (2015).

[10] L. Z. Zhang, Z. F. Wang, Z. M. Wang, S. X. Du, H. J. Gao, and F. Liu, Highly anisotropic Dirac fermions in square graphynes, J. Phys. Chem. Lett. **6**, 2959 (2015).

[11] B. Feng, J. Zhang, S. Ito, M. Arita, C. Cheng, L. Chen, K. Wu, F. Komori, O. Sugino, K. Miyamoto *et al.*, Discovery of 2d anisotropic Dirac cones, Adv. Mater. **30**, 1704025 (2018).

[12] C. Niu, P. M. Buhl, G. Bihlmayer, D. Wortmann, Y. Dai, S. Blügel, and Y. Mokrousov, Two-dimensional topological nodal line semimetal in layered X_2Y (X = Ca, Sr, and Ba; Y = As, Sb, and Bi), Phys. Rev. B **95**, 235138 (2017).

[13] B. Yang, X. Zhang, and M. Zhao, Dirac node lines in two-dimensional Lieb lattices, Nanoscale **9**, 8740 (2017).

[14] H. L. Lu, W. Luo, X. Y. Li, S. Q. Yang, J. X. Cao, X. G. Gong, and H. J. Xiang, Two-dimensional node-line semimetals in a honeycomb-Kagome lattice, Chin. Phys. Lett. **34**, 057302 (2017).

[15] S. Banerjee, R. R. P. Singh, V. Pardo, and W. E. Pickett, Tight-Binding Modeling and Low-Energy Behavior of the Semi-Dirac Point, Phys. Rev. Lett. **103**, 016402 (2009).

[16] V. Pardo and W. E. Pickett, Half-Metallic Semi-Dirac-Point Generated by Quantum Confinement in TiO_2/VO_2 Nanostructures, Phys. Rev. Lett. **102**, 166803 (2009).

[17] J. Kim, S. S. Baik, S. H. Ryu, Y. Sohn, S. Park, B. G. Park, J. Denlinger, Y. Yi, H. J. Choi, and K. S. Kim, Observation of

tunable band gap and anisotropic Dirac semimetal state in black phosphorus, Science **349**, 723 (2015).

[18] H. Zhang, Y. Xie, Z. Zhang, C. Zhong, Y. Li, Z. Chen, and Y. Chen, Dirac nodal lines and tilted semi-Dirac cones coexisting in a striped boron sheet, J. Phys. Chem. Lett. **8**, 1707 (2017).

[19] B. Feng, B. Fu, S. Kasamatsu, S. Ito, P. Cheng, C.-C. Liu, Y. Feng, S. Wu, S. K. Mahatha, P. Sheverdyaeva *et al.*, Experimental realization of two-dimensional Dirac nodal line fermions in monolayer Cu_2Si, Nat. Commun. **8**, 1007 (2017).

[20] X. P. Li, B. Fu, D. S. Ma, C. X. Cui, Z. M. Yu, and Y. G. Yao, Double Dirac nodal line semimetal with a torus surface state, Phys. Rev. B **103**, L161109 (2021).

[21] T. R. Chang, I. Pletikosic, T. Kong, G. Bian, A. Huang, J. Denlinger, S. K. Kushwaha, B. Sinkovic, H. T. Jeng, T. Valla *et al.*, Realization of a type-II nodal-line semimetal in Mg_3Bi_2, Adv. Sci. (Weinheim, Ger.) **6**, 1800897 (2019).

[22] J. He, X. Kong, W. Wang, and S. P. Kou, Type-II nodal line semimetal, New J. Phys. **20**, 053019 (2018).

[23] P. Adroguer, D. Carpentier, G. Montambaux, and E. Orignac, Diffusion of Dirac fermions across a topological merging transition in two dimensions, Phys. Rev. B **93**, 125113 (2016).

[24] H. Isobe, B. J. Yang, A. Chubukov, J. Schmalian, and N. Nagaosa, Emergent Non-Fermi-Liquid at the Quantum Critical Point of a Topological Phase Transition in Two Dimensions, Phys. Rev. Lett. **116**, 076803 (2016).

[25] P. Dietl, F. Piéchon, and G. Montambaux, New Magnetic Field Dependence of Landau Levels in a Graphenelike Structure, Phys. Rev. Lett. **100**, 236405 (2008).

[26] P. Delplace and G. Montambaux, Semi-Dirac point in the Hofstadter spectrum, Phys. Rev. B **82**, 035438 (2010).

[27] A. Mawrie and B. Muralidharan, Quantum thermoelectrics based on two-dimensional semi-Dirac materials, Phys. Rev. B **100**, 081403(R) (2019).

[28] L. Gao, J. T. Sun, J. C. Lu, H. Li, K. Qian, S. Zhang, Y. Y. Zhang, T. Qian, H. Ding, X. Lin *et al.*, Epitaxial growth of honeycomb monolayer CuSe with Dirac nodal line fermions, Adv. Mater. **30**, 1707055 (2018).

[29] R. W. Zhang, C. C. Liu, D. S. Ma, and Y. Yao, From node-line semimetals to large-gap quantum spin Hall states in a family of pentagonal group-IVA chalcogenide, Phys. Rev. B **97**, 125312 (2018).

[30] R. Zhang, Z. Li, and J. Yang, Two-dimensional stoichiometric boron oxides as a versatile platform for electronic structure engineering, J. Phys. Chem. Lett. **8**, 4347 (2017).

[31] B. Wang, H. Gao, Q. Lu, W. H. Xie, Y. Ge, Y. H. Zhao, K. Zhang, and Y. Liu, Type-I and type-II nodal lines coexistence in the antiferromagnetic monolayer $CrAs_2$, Phys. Rev. B **98**, 115164 (2018).

[32] H. Chen, S. Zhang, W. Jiang, C. Zhang, H. Guo, Z. Liu, Z. Wang, F. Liu, and X. Niu, Prediction of two-dimensional nodal-line semimetals in a carbon nitride covalent network, J. Mater. Chem. A **6**, 11252 (2018).

[33] Y. Hasegawa, R. Konno, H. Nakano, and M. Kohmoto, Zero modes of tight-binding electrons on the honeycomb lattice, Phys. Rev. B **74**, 033413 (2006).

[34] P. Kim and C. H. Park, The electronic structure and intervalley coupling of artificial and genuine graphene superlattices, Nano Res. **9**, 1101 (2016).

[35] Q. Zhong, K. Niu, L. Chen, H. Zhang, D. Ebeling, J. Björk, K. Müllen, A. Schirmeisen, and L. Chi, Substrate-modulated synthesis of metal–organic hybrids by tunable multiple aryl–metal bonds, J. Am. Chem. Soc. **144**, 8214 (2022).

[36] G. Kresse and J. Furthmüller, Efficient iterative schemes for ab initio total-energy calculations using a plane-wave basis set, Phys. Rev. B **54**, 11169 (1996).

[37] G. Kresse and D. Joubert, From ultrasoft pseudopotentials to the projector augmented-wave method, Phys. Rev. B **59**, 1758 (1999).

[38] J. P. Perdew, K. Burke, and M. Ernzerhof, Generalized Gradient Approximation Made Simple, Phys. Rev. Lett. **77**, 3865 (1996).

[39] J. Heyd, G. E. Scuseria, and M. Ernzerhof, Hybrid functionals based on a screened Coulomb potential, J. Chem. Phys. **118**, 8207 (2003).

[40] Z. Aizenshtat, Perylene and its geochemical significance, Geochim. Cosmochim. Acta **37**, 559 (1973).

[41] B. Silvi and A. Savin, Classification of chemical bonds based on topological analysis of electron localization functions, Nature (London) **371**, 683 (1994).

[42] S. Zhang, J. Zhou, Q. Wang, X. Chen, Y. Kawazoe, and P. Jena, Penta-graphene: A new carbon allotrope, Proc. Natl. Acad. Sci. USA **112**, 2372 (2015).

[43] R. C. Andrew, R. E. Mapasha, A. M. Ukpong, and N. Chetty, Mechanical properties of graphene and boronitrene, Phys. Rev. B **85**, 125428 (2012).

[44] E. Cadelano, P. L. Palla, S. Giordano, and L. Colombo, Elastic properties of hydrogenated graphene, Phys. Rev. B **82**, 235414 (2010).

[45] D. Zhao, L. Cui, J. Cai, Y. Guo, X. Cui, T. Song, and Z. Liu, Palgraphyne: A promising 2D carbon Dirac semimetal with strong mechanical and electronic anisotropy, Phys. Status Solidi RRL **14**, 1900670 (2020).

[46] H. Liu, J. T. Sun, C. Cheng, F. Liu, and S. Meng, Photoinduced Nonequilibrium Topological States in Strained Black Phosphorus, Phys. Rev. Lett. **120**, 237403 (2018).

[47] H. Huang, K. H. Jin, and F. Liu, Black-hole horizon in the Dirac semimetal $Zn_2In_2S_5$, Phys. Rev. B **98**, 121110(R) (2018).

[48] B. Zheng, B. Xia, R. Wang, Z. Chen, J. Zhao, Y. Zhao, and H. Xu, Ideal type-III nodal-ring phonons, Phys. Rev. B **101**, 100303(R) (2020).

[49] Z. Liu, H. Xin, L. Fu, Y. Liu, T. Song, X. Cui, G. Zhao, and J. Zhao, All-Silicon Topological Semimetals with Closed Nodal Line, J. Phys. Chem. Lett. **10**, 244 (2019).

[50] H. Weng, X. Dai, and Z. Fang, Topological semimetals predicted from first-principles calculations, J. Phys.: Condens. Matter **28**, 303001 (2016).

[51] See Supplemental Material at http://link.aps.org/supplemental/10.1103/PhysRevB.106.195429 for electronic band structures of Ag_3C_{20} ML from different methods (Fig. S1), the orbital and atom decomposed bands with irreducible representations around the Dirac points of D_3, D_4, and D_5 (Fig. S2), the irreducible representations and mirror eigenvalues for all the occupied bands at d_1 and d_2 (Table S1), electronic band structures of Ag_3C_{20} MLs under biaxial strains (Fig. S3), uniaxial *b* strains (Fig. S4), and uniaxial *a* strains (Fig. S5) from −5% to 5%, electronic band structures of Ag_3C_{20} ML under −3% biaxial strain along different paths (Fig. S6), the orbital and atom decomposed bands of B1, B2, and B3 (Fig. S7).

[52] J. Gao, Q. Wu, C. Persson, and Z. Wang, Irvsp: To obtain irreducible representations of electronic states in the VASP, Comput. Phys. Commun. **261**, 107760 (2021).

[53] L. Elcoro, B. Bradlyn, Z. Wang, M. G. Vergniory, J. Cano, C. Felser, B. A. Bernevig, D. Orobengoa, G. Flor, and M. I. Aroyo, Double crystallographic groups and their representations on the Bilbao Crystallographic Server, J. Appl. Crystallogr. **50**, 1457 (2017).

[54] C. Fang, H. Weng, X. Dai, and Z. Fang, Topological nodal line semimetals, Chin. Phys. B **25**, 117106 (2016).

[55] L. Cui, T. Song, J. Cai, X. Cui, Z. Liu, and J. Zhao, Three-dimensional borophene: A light-element topological nodal-line semimetal with direction-dependent type-II Weyl fermions, Phys. Rev. B **102**, 155133 (2020).

[56] S. Deng, A. V. Sumant, and V. Berry, Strain engineering in two-dimensional nanomaterials beyond graphene, Nano Today **22**, 14 (2018).

[57] C. Si, Z. Sun, and F. Liu, Strain engineering of graphene: A review, Nanoscale **8**, 3207 (2016).